Coastal Engineering 128 (2017) 44–57

Contents lists available at ScienceDirect

Coastal Engineering

journal homepage: www.elsevier.com/locate/coastaleng

An experimentally validated approach for evaluating tsunami inundation forces on rectangular buildings

A.S.J. Foster [a,*], T. Rossetto [a], W. Allsop [b]

[a] University College London, London, UK
[b] HR Wallingford, Wallingford, UK

A B S T R A C T

This paper presents an experimentally validated, closed-form set of equations for predicting forces on rectangular buildings impinged by nominally unsteady tsunami inundation flows. The shallow water waves that drive the tsunami inundation flows described in this paper are generated using a novel tsunami simulator, uniquely capable of generating very long period waves featuring the characteristic draw-down of real-world tsunami. We describe an experimental study of the forces acting on a rectangular building occupying 10–80% of a channel, fixed in a free-surface-channel flow driven by shallow water waves with periods of 20–240 s. An idealised topography and a 1:50 Froude scale are adopted. A one dimensional model based upon open-channel flow principles is proposed for unsteady flows driven by prototype tsunami waves, providing empirical estimates for drag and hydrostatic coefficients. It is observed that the pressure field around the buildings is hydrostatic irrespective of the flow being steady or unsteady. An empirically derived force prediction equation, dependent upon the Froude number of the incoming flow and blocking fraction is presented, which provides good agreement with the experimental results. The equations presented in this paper will provide engineers, tsunami modellers, and risk evaluation experts with a convenient method of tsunami inundation force determination without recourse to computationally expensive multi-scale numerical models.

1. Introduction and background

The Japan (2011) and Indian Ocean (2004) tsunami resulted in significant loss of life, buildings, and critical infrastructure (EEFIT, 2004; EEFIT, 2009; EEFIT, 2011; EEFIT, 2013). In order to mitigate such losses it is essential to have an understanding of the likely inundation forces that will arise during a tsunami event.

Tsunami inundation forces imposed upon structures in coastal regions are due to the unsteady flow of sea water around them, which may be evaluated as a combination of drag, hydrostatic and inertia forces. Related studies (Qi et al., 2014; Bahmanpour et al., 2017) have evaluated tsunami inundation forces using steady flow data, but these do not consider the evolution of these forces during a tsunami event. It is important to consider unsteady flow in order to gain a complete understanding of the temporal evolution of water surface elevation, velocity, pressure, and total inundation force around the structure. This paper addresses the interaction between unsteady flow due to prototype tsunami waves with periods between 20 and 240 s, and a rectangular surface-piercing rigid obstacle. The wave periods considered are classified as either quasi-steady or unsteady according to the magnitude of their flow accelerations. New and detailed laboratory data is presented and a semi-empirical model for predicting the forces experienced by the obstacle is proposed.

The current literature on tsunami inundation forces on buildings is somewhat disparate. This reflects the relatively broad range of areas within fluid mechanics from which current research draws, and the assumptions made in modelling the tsunami inundation flows. Over the past few decades, research has focused upon: (1) determining the pressure field of the impinging tsunami wave through shallow water theory (Ritter, 1892; Vallis, 2006); (2) characterising the flow as either steady or unsteady, subcritical or supercritical (Qi et al., 2014; Bahmanpour et al., 2017); and (3) investigating the local interactions between obstacles and the flow (Fenton et al., 2003, 2008). The combined effect of all of these components, coupled with and validated against realistic prototype tsunami conditions, has not yet been investigated widely.

Early theoretical work that may be related to the determination of pressure fields of tsunami is that of Ritter (1892), who conducted work on propagating bores and presented solutions to the non-linear shallow water equations for a dam break of inviscid flow over a dry bed. More general forms of the shallow water equations (see Dean and Dalrymple (1984)) demonstrate that the resulting pressure field is hydrostatic. As a result, open-channel flow principles, which assume hydrostatic pressure distributions, may be used to analyse local variations in surface conditions. Initial analytical studies by Escande (1939) examined the problem

* Corresponding author.
E-mail address: a.foster@ucl.ac.uk (A.S.J. Foster).

http://dx.doi.org/10.1016/j.coastaleng.2017.07.006
Received 16 November 2016; Received in revised form 12 April 2017; Accepted 28 July 2017
Available online 4 August 2017

of interactions between obstacles and channel flow using energy principles, but their generality was limited by arbitrary theoretical closures.

More recently, there has been movement towards momentum and drag concepts, which can be used to determine the criticality of the flow. Hsieh (1964) conducted a preliminary investigation into the resistance coefficients of cylinders in a rectangular channel, which were shown to be a function of the Froude number, the relative depth of the incoming flow, and the relative spacing of the piers; the direct effect of the piers on the free surface was however neglected. Henderson (1966) describes, but does not present a solution to, an approach that uses the momentum principle to provide an estimate for the perturbed water depth. Ranga Raju et al (Ranga Raju et al., 1983). and Montes (1998) developed polynomial approximations for the change in water depth due to the presence of cylindrical piers, but this analysis is restricted by the assumption that changes in water depth are small and the flow conditions are subcritical. More recent experimental work Arnason et al. (2009). and Qi et al. (2014). has demonstrated that under certain circumstances choked flow can result, leading to large changes in water depth.

There have been numerous experimental investigations examining the effects of surface-piercing obstructions on the free surface profile up and downstream of the obstruction in open channels under steady conditions (Dargahi, 1989; Sadeque et al., 2008; Reinauer and Hager, 1994). For unsteady conditions, preliminary investigations have focused upon bores and hydraulic jumps in unobstructed channels (Yeh et al., 1989; Hornung et al., 1995; Svendsen et al., 2000). Subsequent research has examined the forces imparted by a bore on a rigid structure and the simultaneous effect of the structure on the flow of the bore (Cross, 1967; Fukui et al., 1963; Nakamura and Tsuchiya, 1973; Asakura et al., 2002; Ramsden and Raichlen, 1990; Ramsden, 1993). Most experimental studies regarding tsunami are limited to simulating these waves with either solitary waves or bores generated by a dam break (Lukkunaprasit et al., 2009; Thusyanthan and Madabhushi, 2008). Furthermore, the waves simulated in these studies are generally of a short wave period, resulting in a gap in the literature (see Fig. 1). This paper presents experiments that follow a more recent approach, whereby tsunami simulation is achieved by means of a volume-driven wave-maker that releases a column of water of a specified volume at a controlled rate, as described by Rossetto et al. (2011). and McGovern et al. (2017). This approach has the advantage of being able to generate both trough- and crest-led waves of periods between 20 and 240 s, which are significantly longer than any other waves produced under laboratory conditions to date.

Practical guidance on the design of buildings against tsunami action effects are provided in documentation produced by various federal and national agencies. These include the Federal Emergency Management Agency FEMA P-646 guidelines (FEMA, 2012) and the Building Center of Japan guidelines (Okada et al., 2004), which adopt different methods for

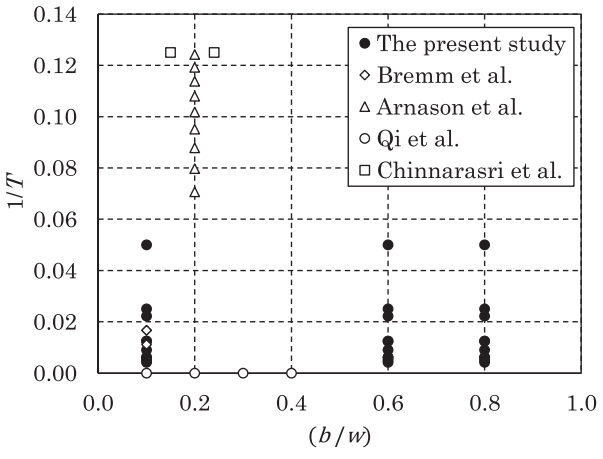

Fig. 1. Variations of blocking fraction with wave period (the present study and related studies).

estimating inundation pressures and total forces. The procedure proposed by FEMA (FEMA, 2012) initially assumes a maximum run-up value R, from which a maximum water height h_{max} can be determined. The hydrostatic force F_h for a fully submerged wall of height h_w and width b is then determined as:

$$F_h = \rho g\left(h_{max} - \frac{h_w}{2}\right) b h_w \tag{1}$$

in which ρ is the density of sea water and g is the gravitational acceleration. Hydrodynamic or drag forces F_d for a building with a drag coefficient C_D subjected to an inundation flow velocity u are calculated as:

$$F_d = \rho C_D B\left(hu^2\right) \tag{2}$$

from which impulsive forces F_s are determined as:

$$F_s = 1.5F_d \tag{3}$$

A recent update to the ASCE 7 standard (ASCE/SEI 7-16, 2017) also incorporates the same impulse magnification of $1.5F_d$ as described by Eq. (3) into the hydrodynamic force definition. However, the guidelines allow for this to be omitted when a bore is dissipated by topography, and when the inundation flow is characterised by a Froude number less than one. The methodologies described by (FEMA, 2012) and (ASCE/SEI 7-16, 2017) assume that the impulsive, hydrodynamic, and hydrostatic forces can be decoupled and they further neglect the effect of the presence of the building on the flow conditions. Research by Qi et al. (2014). and Bahmanpour et al. (2017). have shown that the flow, pressure distribution and forces are all sensitive to the presence of buildings. Furthermore, for very long period inundation flows, the experiments presented in this paper and in (McGovern et al., 2017) show that an initial impulsive force component may not occur (see Section 4) or be a prerequisite for accurate force determination.

This paper presents an extension of previous research into the subject of tsunami inundation forces presented in Qi et al. (2014). and Bahmanpour et al. (2017). Qi et al. (2014). propose force equations for steady flows around objects based on small-scale experiments, with Bahmanpour et al. (2017). extending the work of Qi et al. (2014). through a numerical investigation. Here, the steady flow force equations are tested against large-scale tsunami tests and hence this paper introduces unsteady flow to tsunami inundation force problems.

This paper has two primary aims. Firstly, to describe the evolution of pressures and forces of tsunami inundation flows around a single rigid rectangular object. Secondly, to develop a semi-empirical force equation in terms of offshore water height, flow velocity, blocking fraction, and Froude number with a view to being used in future design codes and numerical models. To these ends, we describe a detailed experimental study of the forces acting on a square obstacle, over a range of blocking fractions, due to waves of various periods that simulate prototype-like tsunami. We adapt these experiments first to check whether the one-dimensional model by Qi et al. (2014). for quasi-steady flow conditions produces a good prediction of the measured forces. We then propose a modified version of these equations with a new empirical closure.

2. Analytical framework

The adoption of an analytical framework for force determination based on unsteady flows around surface-piercing objects assumes the inundation imposed by tsunami is quasi-steady. Fig. 2a shows the variation of vertical water particle velocity with surface elevation as a function of time for one of the waves considered in Section 3 of this study (wave period T = 80 s). Readings shown are for the shoreline (x = 84.93 m) and far offshore (x = 10.93 m), in which x is the distance from the front of the tsunami simulator. The figure shows that, excluding the transition phase between the wave advancing and receding, the water particle velocity remains constant with surface elevation. This suggests a

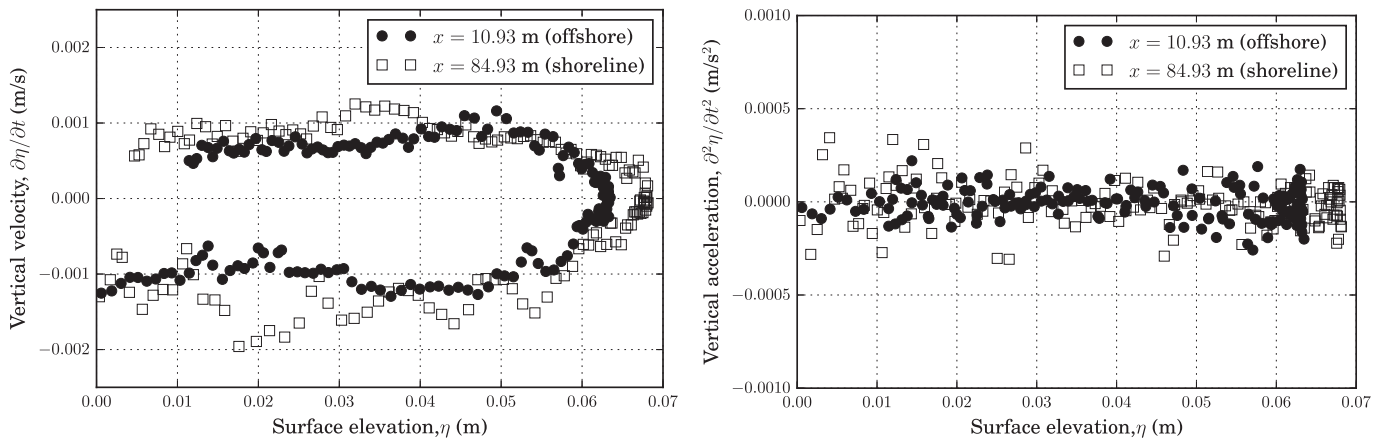

(a) Velocity. (b) Acceleration.

Fig. 2. Spatial variation of vertical water particle velocity and acceleration with surface elevation as a function of time.

steady flow characteristic. Furthermore, between the two extreme locations, the velocity profiles are similar, suggesting that there is little spatial variation of the flow. Considering the accelerations presented in Fig. 2b, these are appreciably close to zero and corroborate the observations drawn from Fig. 2a. These initial observations suggest that adopting a starting assumption of quasi-steady flow can be justified for predicting inundation forces that are driven by nominally unsteady flow due to long waves typical of tsunami.

The most relevant aspects of the experimental conditions generated in this study can be modelled using long-wave theory to predict the pressure field, and the momentum principle to determine the criticality of the flow and hence the position of the free surface.

Tsunami waves and other waves with extremely long periods and wavelengths are referred to in the literature as long or shallow water waves (Dean and Dalrymple, 1984). Fig. 3 describes a long wave of wavelength L, amplitude $H/2$, horizontal (x-direction) velocity u vertical (z-direction) velocity w, and surface profile η impinging upon an obstacle of length l and width b immersed in initially still water of depth h. From small amplitude wave theory, the surface profile and velocities for a progressive wave of period T are described by:

$$u = \frac{H}{2}\frac{gk}{\sigma}\frac{\cosh k(h+z)}{\cosh kh}\cos(kx-\sigma t) \tag{4a}$$

$$w = \frac{H}{2}\frac{gk}{\sigma}\frac{\sinh k(h+z)}{\cosh kh}\sin(kx-\sigma t) \tag{4b}$$

$$\eta = \frac{H}{2}\cos(kx-\sigma t) \tag{4c}$$

In these equations $k = (2\pi/L)$ is the wave number, $\sigma = (2\pi/T)$ is the angular frequency and g is the gravitational acceleration. For $kh \ll \pi/10$ the asymptotic forms of the hyperbolic functions in Equations (4a) and (4b) are $\cosh kh = 1$ and $\sinh kh = kh$ respectively, resulting in shallow water particle velocities u_s and w_s:

$$u_s = \frac{gHk}{2\sigma}\cos(kx-\sigma t) = \frac{\eta C}{h} \tag{5a}$$

$$w_s = \frac{gHk}{2\sigma}[k(h+z)]\sin(kx-\sigma t) = -C\left(1+\frac{z}{h}\right)\frac{\partial\eta}{\partial x} \tag{5b}$$

in which $C = \sqrt{gh}$ is the shallow water celerity. The pressure field p associated with a progressive wave is determined from the unsteady Bernoulli equation, whose velocity potential ϕ is given by:

$$\phi = \frac{H}{2}\frac{g}{\sigma}\frac{\cosh k(h+z)}{\cosh kh}\sin(kx-\sigma t) \tag{6}$$

which results in:

$$p = \rho g z + \rho g\eta\frac{\cosh k(h+z)}{\cosh kh} \tag{7}$$

in which ρ is the fluid density. For shallow water conditions where $kh \ll \pi/10$:

$$p = \rho g z + \rho g\eta = \rho g(\eta - z) \tag{8}$$

Thus the pressure due to long waves is hydrostatic, since the vertical accelerations can be shown to be small (Dean and Dalrymple, 1984); this is shown to be true for sea walls completely blocking the flume in related experimental work by McGovern et al. (2016). With reference to the pressure distributions p_1 and p_2 in Fig. 3, the net force F_x in the x-direction is defined as:

$$\begin{aligned} F_x &= P_1 - P_2 \\ &= \int_{-S}^{-S+h1} bp_1(x_1,z,t)\mathrm{d}z - \int_{-S}^{-S+h2} bp_2(x_1+l_1,z,t)\mathrm{d}z \end{aligned} \tag{9}$$

in which $-S$ is the bed surface elevation. Hence for long waves, the problem of determining the net force on a building is reduced to knowing the relationship between the upstream and downstream water depths h_1 and h_2. Since there is an absence of dynamic pressure in long waves, h_1 and h_2 can be determined using steady open channel flow principles.

Current practice in tsunami inundation force determination is typically reliant upon numerical models that calculate inundation flow velocities in preparation for drag force computations (Imamura and Imteaz,

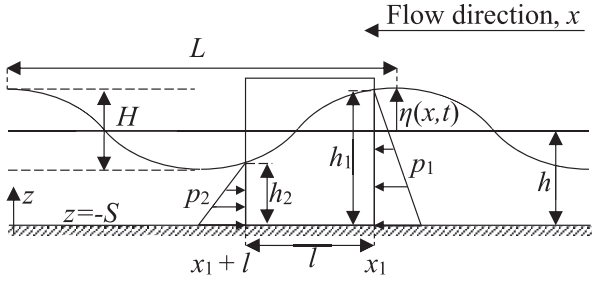

Fig. 3. Schematic of an obstacle of width b, partially immersed by a long wave of wavelength L, and amplitude $H/2$.

1995; Synolakis et al., 2008). The influence of buildings upon inundation flows is then determined indirectly through an appropriate velocity adjustment, incorporating an empirical roughness coefficient (see Gauckler (1867) and Manning (1891)). This paper proposes an alternative approach and examines the applicability of an analytical framework that directly considers the presence of buildings on the inundation flow. In this framework, forces on an object or building are critically dependent upon knowledge of the upstream and downstream Froude numbers, Fr_1 and Fr_2 respectively. This implies that an estimate of these forces can be derived by considering the influence of the object in a channel upon the height h of the free surface. Through an experimentally determined empirical closure, the need to explicitly take into account the presence of the building is negated, which permits the forces acting on a building at any given location in the inundation flow to be determined knowing only the Froude number and building dimensions. This is advantageous for numerical modelling as the presence of a building will not need to be taken into account. It is also of practical relevance for engineering calculations and risk evaluations that seek to take advantage of historic or site-specific environmental data without recourse to costly numerical models.

The idealisation originally used to develop this framework by Qi et al. (2014). is summarised in Fig. 4, and comprises a flow in a rectangular channel of depth h and an average uniform velocity of u. The unobstructed channel has a width w, which upon introducing an obstacle of width b, is constricted to a net width of $(w-b)$. The total force $\overline{F}_D$ on the obstacle can be calculated in terms of the fluid density ρ, the drag coefficient C_D, the hydrostatic coefficient C_H, gravitational acceleration g, the wetted frontal area of the obstacle $A = bh$, the net water surface elevation (h_1-h_d), and the local mean horizontal fluid velocity u:

$$\overline{F}_D = \frac{1}{2}C_D\rho b u^2 h + \frac{1}{2}C_H\rho b g\left(h_1^2 - h_d^2\right) \tag{10}$$

For a fixed control volume CV, the Reynolds transport theorem gives the linear momentum relation (Reynolds, 1903):

$$\sum \mathbf{F} = \frac{\mathrm{d}}{\mathrm{d}t}\left(\int_{\mathrm{CV}} \mathbf{u}\rho \mathrm{d}V\right) + \int_{s_1+s_d} \mathbf{u}\rho(\mathbf{u}\cdot\hat{\mathbf{n}})\mathrm{d}A \tag{11}$$

in which $\hat{\mathbf{n}}$ is the outward normal unit vector and $\Sigma\mathbf{F}$ is the vector sum of surface tractions on all fluids and solids cut by the control surface, as well as all body forces acting on the masses within the control volume. Assuming a locally steady one-dimensional flow, $\mathrm{d}/\mathrm{d}t = 0$, the right-hand side of Eq. (11) may be written as:

$$\int_{s_1+s_d} \mathbf{u}\rho(\mathbf{u}\cdot\hat{\mathbf{n}})\mathrm{d}A = u_1\rho_1 u_1 A_1 - u_d\rho_d u_d A_d \tag{12}$$

Assuming incompressible flow $\rho_1 = \rho_d = \rho$ and invoking the continuity equation such that $\rho u_1 A_1 = \rho u_d A_d$:

$$\int_{s_1+s_d} \mathbf{u}\rho(\mathbf{u}\cdot\hat{\mathbf{n}})\mathrm{d}A = \rho u_1 A_1(u_1 - u_d) = \rho Q(u_1 - u_d) = \rho(M_1 - M_d) = \overline{F} \tag{13}$$

in which $Q = uwh$ is the volume flux and M is the momentum flux at the control surfaces. Fenton (Fenton et al., 2003) defines the momentum flux as:

$$M = \left(gAh_c + \beta\frac{Q^2}{A}\right) \tag{14}$$

in which h_c is the depth of the centroid of the section below the surface such that $Ah_c = (1/2)h^2 w$, and β is the Boussinesq coefficient $\beta = (A/Q^2)\int_A u^2 \mathrm{d}A$, which takes into account non-uniform velocity over the cross-section. For regular channels, flumes and spillways, $\beta = 1.03$ (Chow, 1959), which for the purposes of this paper is approximated to $\beta = 1$. The upstream Froude number Fr_1 is defined as

$$Fr = \frac{u_1}{\sqrt{gh_1}}. \tag{15}$$

When Fr_1 is less than a critical value Fr_{1c}, the upstream flow is seen by Qi et al. (2014). to be subcritical. For Fr_1=Fr_{1c}, the downstream Froude number jumps to $Fr_{2c} > 1$, corresponding to a choked flow where the momentum loss is greatest. For choked flows, the flow downstream of the building is characterised by a hydraulic jump, across which there is a change in water depth. To determine the flow state Fr_d downstream of the buildings, Eqs. (13)–(15) can be used to form a relationship between Fr_1 and Fr_d in terms of C_D, (b/w), and C_H:

$$\left(1 - \frac{C_H b}{w}\right)\frac{1}{2Fr_1^{4/3}} + \left(1 - \frac{C_D b}{2w}\right)Fr_1^{2/3} = \left(1 - \frac{C_H b}{w}\right)\frac{1}{2Fr_d^{4/3}} + Fr_d^{2/3} \tag{16}$$

which is a transcendental equation. In the presence of supercritical flow ($Fr_1 > 1$), the far downstream Froude number Fr_2 is evaluated by first determining the conjugate depths h_d/h_2:

$$\frac{h_d}{h_2} = \frac{1}{2}\sqrt{1 + 8Fr_d^2 - 1} \tag{17}$$

From the continuity equation $u_2 = u_d\,(h_d/h_2)$, which yields the far downstream Froude number Fr_2:

$$Fr_2 = \frac{2^{3/2}}{\left(\sqrt{1 + 8Fr_d^2 - 1}\right)^{3/2}} \tag{18}$$

Fig. 5 plots the relationship between Fr_1 and Fr_2 for the blocking fractions ($b/w = 0.1, 0.6, 0.8$) considered in this study. This figure shows that below a subcritical upstream Froude number (Fr_1<Fr_c), Fr_1 and Fr_2 are correlated, such that the difference between upstream and downstream water height is small. At Fr_1=Fr_c, the downstream Froude number jumps to Fr_{2c}, such that the water depth decreases rapidly around the sides of the obstacle and a hydraulic jump forms downstream. This figure assumes a hydrostatic coefficient $C_H = 0.58$ (Qi et al., 2014) and a drag coefficient C_D:

$$C_D = C_{D0}\left(1 + \frac{C_{D0} b}{2w}\right)^2 \tag{19}$$

where C_{D0} is the drag coefficient for unbounded flow, equal to 1.9 when ambient turbulence is taken into account (Tamura and Miyagi, 1999).

The framework described will be extended, using new experimental

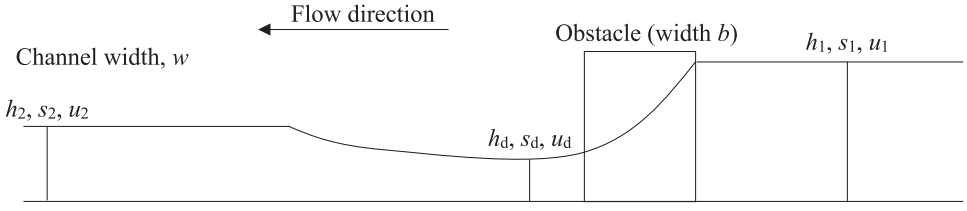

Fig. 4. Schematic of an obstacle of width b constricting an open channel of width w containing a choked free surface flow with local velocities u_i, water depths h_i, and control surfaces s_i.

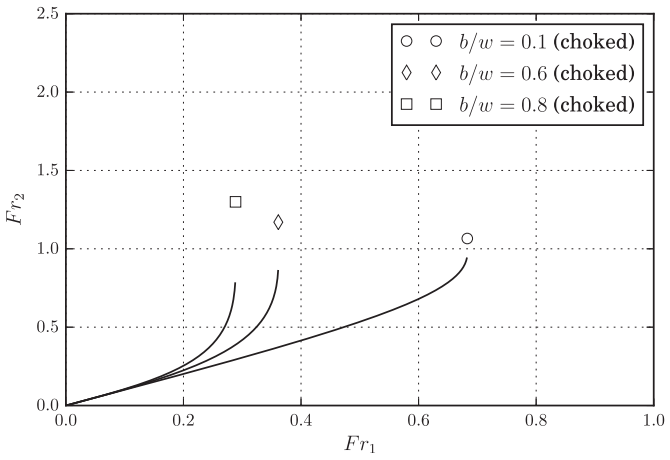

Fig. 5. Model predicted relationship between Fr_1 and Fr_2 for the range of parameters used in the present study.

data, to examine the influence of unsteady flow on the inundation forces experienced by rectangular buildings and to provide a set of semi-empirical equations for force prediction.

3. Experimental study

To examine the influence of unsteady flow on forces experienced by rectangular buildings, an experimental study is conducted where obstacles of varying blocking fractions are subjected to unsteady free-surface-flow driven by trough-led waves (N-waves) and solitary waves. Depending upon the upstream and downstream Froude numbers, the flow regime is classified as either subcritical or choked, according to the thresholds defined by Qi et al. (2014). The presence of a rigid body, introduced into a channel flow, generates a perturbation. At low *Fr*, the difference in water depth upstream and downstream is negligible. But at high *Fr*, a bore initially propagates upstream and downstream of the obstacle when the water is set in motion, leading to a change in water depth upstream and downstream of the obstacle. In a flume of finite length, a reference unperturbed upstream state will be lost, which means that observations are expressed in terms of an upstream Froude number, Fr_1. In this section we describe the experimental variables, test conditions and apparatus, and data processing methods. Given an upstream state characterised by Fr_1, the analytical framework in this paper will determine the downstream state characterised by Fr_2.

3.1. Experimental variables

A summary of the experimental variables considered in this investigation is presented in Table 1:

Two forms of wave are used in this investigation: solitary and trough-led N-waves. Solitary waves (Miles, 1980) are described by:

$$\eta(x,t) = a\left(\frac{1}{\cosh(x - Ct/L)}\right)^2 \tag{20}$$

where η is the surface elevation, x is the horizontal coordinate, t is time, a is the wave amplitude, C is the wave celerity, and L is the length of the wave. Solitary waves have been used in many other experimental and numerical studies (Jensen et al., 2003; Synolakis, 1987; Briggs et al., 1995; Borthwick et al., 2006) as they possess the ability to carry forward momentum and they feature a positive elevation, making them amenable to traditional paddle-driven flumes. However, solitary waves lack the characteristic depression, or draw-down, of real-world tsunami waves (Madsen et al., 2008), which can produce steeper positive wave fronts after the initial depression has passed. This might lead to higher impact forces on an object or a building. This feature of tsunami waves can be modelled by N-waves (Tadepalli and Synolakis, 1994, 1996), whose leading profile is described by:

$$\eta(x) = \left.\frac{\varepsilon_g \cdot H(x - X_2)}{\cosh^2(\gamma(x-\theta))}\right|_t \tag{21}$$

where $\eta(x)$ is the surface elevation, $\varepsilon_g < 1$ is a scaling parameter defining the crest amplitude H, $\theta = X_1 + Ct$ and $L = X_1 - X_2$ (in which X_2 is the x position of the inflexion point of the profile corresponding to $\eta(x = X_2) = 0$ and X_1 is the position of a positive solitary wave of the same amplitude centred on $X = X_1$ at $t = 0$), and $\gamma = \sqrt{3Hv_0/4}$, where v_0 is a steepness parameter set to 1 by (Tadepalli and Synolakis, 1996). Due to its novel method of wave generation, the pneumatic tsunami generator used in this study has the ability to produce waves with a leading trough or depression that are generally not possible with paddle-driven flumes.

The waves generated in this study are not selected to reproduce any particular prototype events, but are generated in the same way and with essentially the same device as experiments that reproduced the Indian Ocean 2004 'Mercator' trace at a Froude scale of 1:50 (Allsop et al., 2014). It may therefore be appropriate to apply that scale in any conversion to prototype. At this scale, scale effects are relatively mild. Surface tension effects will be very small, as will related air entrainment. There will be some effects of relative roughness for the initial stages of flow along the sea bed, but for the later stages of incoming flows of interest here, Reynolds effects will be small.

Table 1
Key experimental variables.

Experimental variable	Values
Flume length, L_f	100 m
Flume width, w	1.8 m
Obstacle widths, b	$b_1 = 0.180$ m, $b_2 = 1.080$ m, $b_3 = 1.440$ m
Blocking fractions, b/w	$b_1/w = 0.1$, $b_2/w = 0.6$, $b_3/w = 0.8$
Wave periods, T	Solitary waves: 20s, 45s, 80s, 160s N-waves: 40s, 80s, 111s, 166s, 200s, 240s

3.2. Experimental set-up

3.2.1. Location

Physical experiments are conducted at HR Wallingford, in a wave tank 100 m long, 1.8 m wide, and of variable depth. The tank is equipped with a wave generator at one end. At the opposite end a 1:20 sloping bathymetry was installed (Fig. 6a), reaching a maximum height of 1 m, the nominal position of the shoreline.

3.2.2. Wave generator

The wave generator in this investigation is of the pneumatic type, referred to herein as a tsunami generator. Unlike wave paddle and plunger wavemakers, a tsunami generator has no moving parts in contact with the water. The design concept behind the tsunami generator is a pump with a low pressure head, connected to a partially immersed plenum chamber, which is open at the bottom and located at one end of the tank. Water drawn into the plenum chamber is released by moving a valve controlled by an electric servo system. The system admits a valve position feedback signal from a transducer at the valve in addition to a reference signal; the system operates an actuator to cause the valve position to match the reference position. The amplitude and frequency of the generated tsunami waves are directly related to the amplitude and frequency of the reference signal. This form of wave generation is ideally suited to simulating tsunami as it allows the controlled movement of large volumes of water in a confined space without high discharge water pumps, which are expensive in both capital and operational costs.

3.2.3. Obstacles

Three rectangular cylinders of constant height h_{box} (0.2 m), depth d_{box}

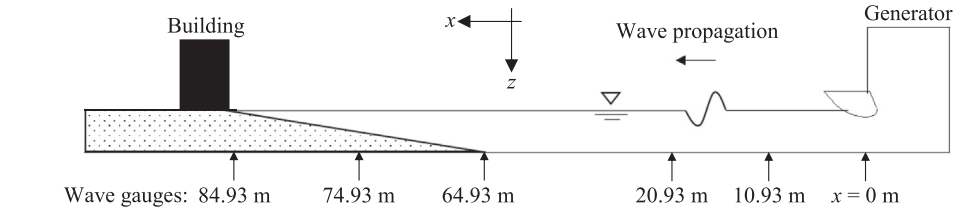

(a) General (longitudinal) arrangement of the test set-up.

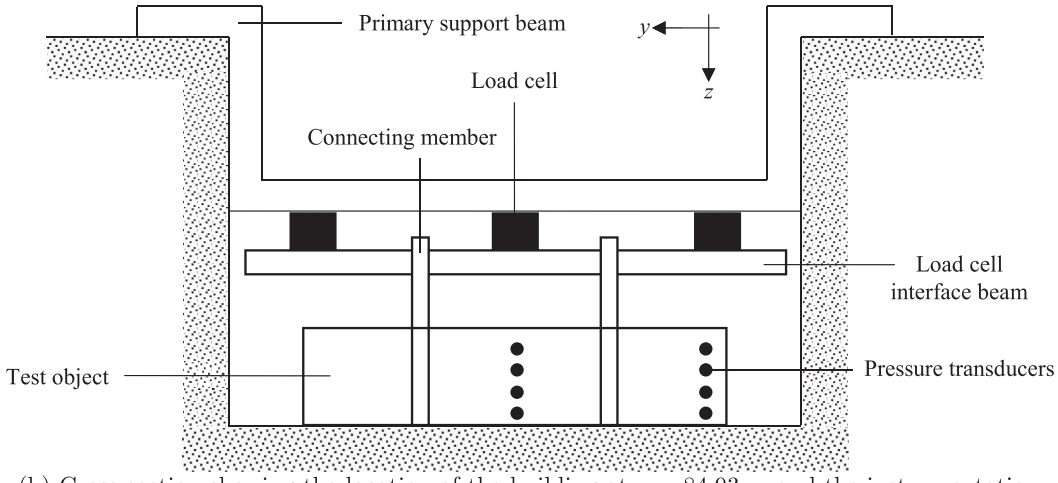

(b) Cross-section showing the location of the building at $x = 84.93$ m and the instrumentation.

Fig. 6. Schematic diagram of the test set-up (not to scale).

(0.18 m), and variable width b (0.18 m, 1.08 m, and 1.44 m) are used in this study. Normalising by the flume width w (1.8 m), these three cylinder widths correspond to blocking fractions b/w 0.1, 0.6, and 0.8. The obstacles are connected to a frame comprising an assemblage of load cells, which in turn connects to a primary support beam attached to the tank side walls (Fig. 6b). The load cells used in these tests are the F232/2 type supplied by Novatech, with a stiffness of 2.1×10^8 N/m, a sampling frequency of 100 Hz and a range of ± 5 kN. The structure is designed to have sufficient stiffness to avoid resonant excitation during the tests. This is verified by measuring the natural frequency of the structure, which is considerably higher than the forcing frequency of the test waves.

3.2.4. Measurement

The water surface elevations η are measured at various locations in the offshore (constant depth region of the flume), the nearshore (above the sloping bathymetry) and onshore (the initially unwetted region beyond the nominal shoreline) using resistive-type wave probes (Fig. 6a). Time series velocity profile data are collected at the bathymetry toe using an acoustic doppler current profiler (ADCP), manufactured by Nortek. Onshore velocity is measured using propeller meters. Pressure is measured using absolute-type pressure gauges, manufactured by Trafag. Pressure gauges of this type are suitable for this investigation due to the relatively low expected dynamic pressures. Readings are taken at four 35 mm intervals along the height of the front face of the obstacles, along the center line in all cases and at an offset for $b/w = 0.6$ and 0.8 (Fig. 6b). Forces are measured using three two-axis strain gauge-type load cells, manufactured by Novatech. The load cells are mounted between the primary support beam and the interface beam in a triangular formation for stability, as well as to minimise any moments due to their position above the obstacle. All of the instrumentation is connected to a data-logger. A trigger system is set up so that when the valve on the tsunami generator is opened, data logging commences instantaneously, with the time set to zero.

3.3. Data processing

Excluding current profile data, which is collected and processed by proprietary software, all data generated during the tests are logged as voltages; the relevant calibration factors are then applied during a post-processing stage to obtain physical quantities. A Fourier smoothing technique is applied to the data generated by the pressure transducers and load cells to remove noisy signal interference.

4. Experimental results

4.1. Wave elevation

Fig. 7a–7d present typical wave surface elevation profiles η for all of the waveforms and periods considered in the present study. These are measured at $x = 64.93$ m (offshore) and $x = 84.93$ m (onshore), which correspond respectively to the start of the bathymetry and the shoreline. Fig. 8a and b presents the evolution of a typical short ($T = 40$ s) and long ($T = 200$ s) N-wave at all instrument locations. In both of the presented cases, as well as all other cases considered, the waveform does not significantly change with position along the offshore region.

Fig. 9 shows the variation of peak water height, recorded at the face of the obstacle, with wave period. It can be seen that the water height ranges from approximately 10%–90% of the height of the obstacle. It is generally observed that higher blocking fractions result in higher measured water levels at the face of the obstacles.

4.2. Regime classification

A key aspect of this research is the influence of unsteady flow conditions upon tsunami forces. As a measure of unsteady flow, second-order time derivatives are taken of the surface elevation η. Although in theory, any time dependency of surface elevation connotes unsteady flow, in practice all flows are locally unsteady even when conditions are

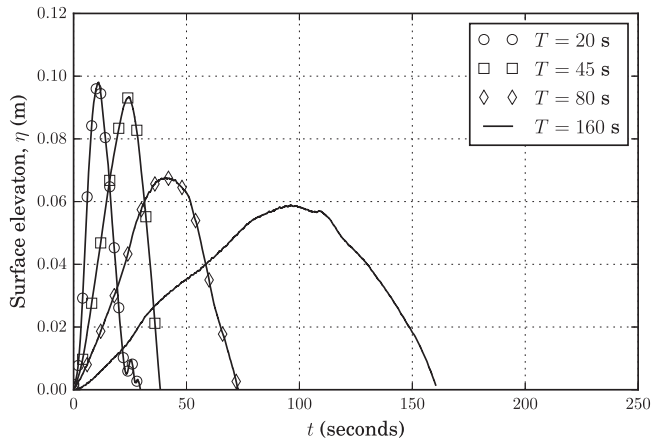

(a) Elevated waves (offshore).

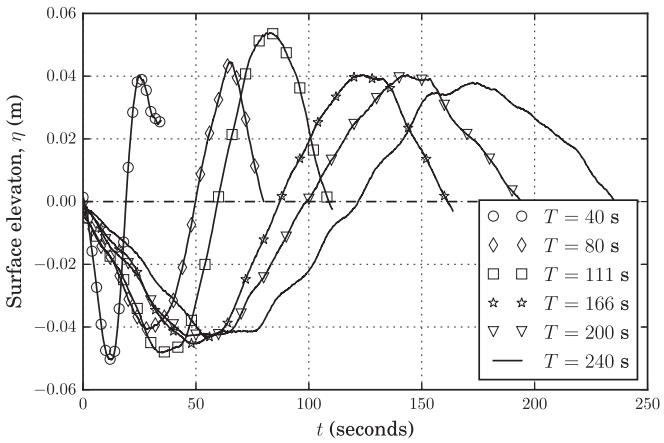

(b) Trough-led waves (offshore).

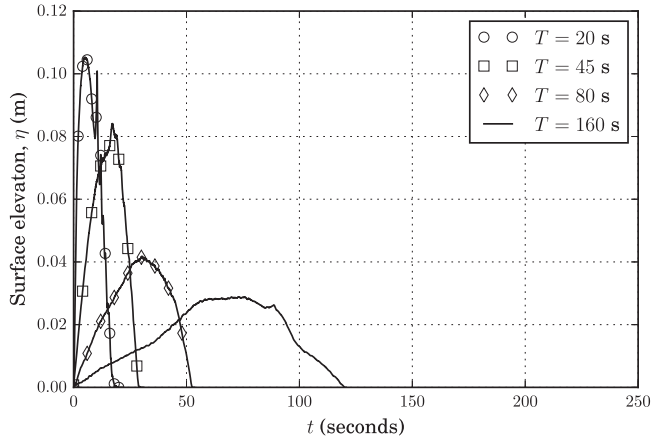

(c) Elevated waves (onshore).

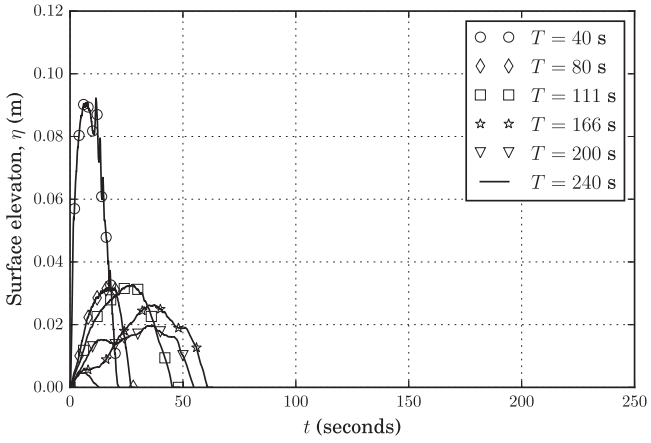

(d) Trough-led waves (onshore).

Fig. 7. Wave profiles measured at a single offshore and onshore location.

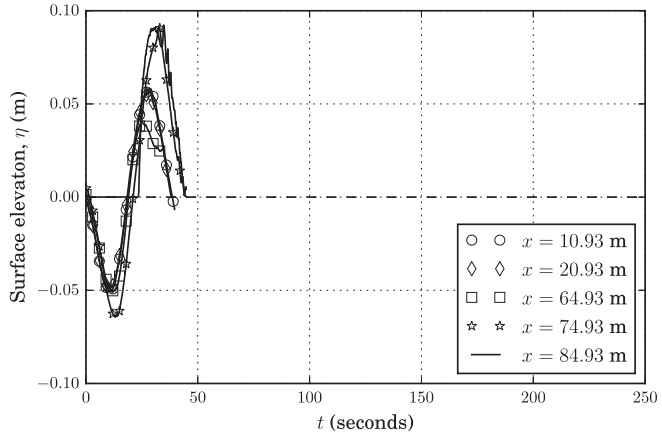

(a) $T = 40$ seconds

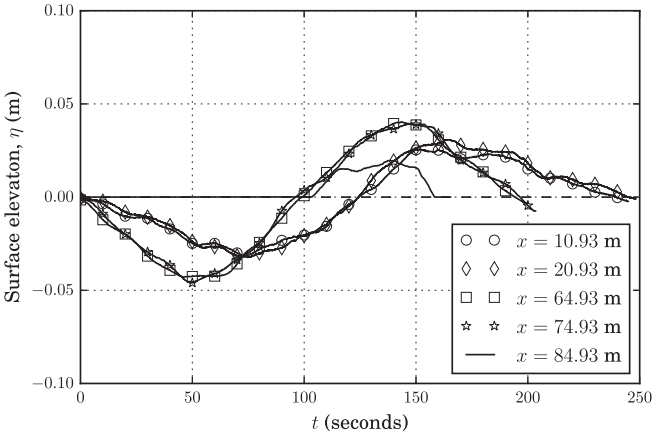

(b) $T = 200$ seconds

Fig. 8. Trough-led N-waves measured at all instrument locations.

considered to be steady in the far-field. For the purposes of this research, the flow will be considered to be unsteady when $\frac{\partial^2 \eta}{\partial t^2}$ is greater than 0.05% of the quantity (h/gl), which corresponds to a term that can adequately non-dimensionalise the water depth time derivative whilst also

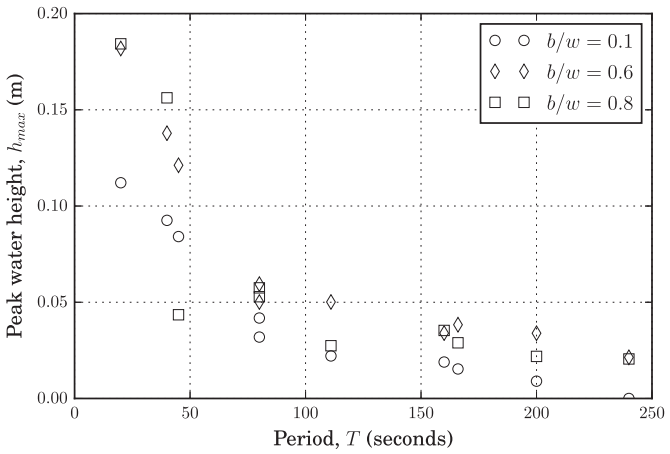

Fig. 9. Variation of peak water height with wave period for all obstacle widths.

encompassing the influence of the length l of the obstacle in the flow. In order to examine the influence of the presence of the building on the flow, the obstacle width b is excluded from the normalisation. Fig. 10a and b shows the relationship between wave period and flow variation, taken at both mean and peak values of $\partial^2\eta/\partial t^2$ (h/gl). Two inferences may be drawn from these figures. Firstly, there is a clear wave period ($T = 80$ s) below which the flow becomes significantly unsteady. Secondly there is a local influence, due to the presence of the obstacle in the flow, that results in higher blocking fractions introducing greater unsteadiness. This is due to higher blocking fractions increasing the tendency of the flow to transition from subcritical to choked. This finding is in accordance with the observations of (Qi et al., 2014) for steady flow, where the blocking fraction (b/w) influences the critical Froude number.

4.3. Velocity, wave celerity and wavelength

Measured and theoretical wave celerity, wavelength and velocity are presented in Table 2 for all waves considered in this study. These data exhibit the anticipated response of an inverse relationship between velocity, wave celerity and wave period (see Fig. 11). A more comprehensive tsunami generator calibration study by (Rossetto et al., 2011) corroborates these results.

With the exception of the $T = 20$s solitary wave, it is noted that for all of the waves considered in this study, the measured wavelength is considerably longer than the flume. This can result in a degree of

Table 2
Key wave parameters.

Period	Celerity	Celerity (theory)	Wavelength	h/L	u_{max}
T (s)	C (m/s)	C_{theory} (m/s)	L (m)		(m/s)
20	3.30	2.44	66.08	0.009	0.85
40	4.63	2.41	185.26	0.003	0.74
45	2.24	2.44	100.60	0.006	0.51
80	2.03	2.36	162.69	0.003	0.74
80	3.05	2.32	244.29	0.002	0.32
111	1.78	2.33	197.15	0.003	0.37
160	1.48	2.33	237.55	0.002	0.16
166	1.72	2.30	285.92	0.002	0.26
200	2.18	2.30	435.06	0.001	0.16
240	2.54	2.30	608.87	0.001	0.22

destructive interference due to wave reflection, which can be observed in Fig. 7b for example, where the reflection of the generated wave begins immediately after the shore-ward motion of fluid from the simulator arrives at the tow of the bathymetry (McGovern et al., 2017). This is expected as both solitary and N-waves carry forward momentum (unlike sine waves, where closed orbital particle paths do not transport mass forwards), which will result in significant reflections from the flume slope. In a related study by McGovern et al. (2017), it is observed that for very long waves, there is an increase in amplitude due to the constructive interference of the prior reflected portions of the wave crest. It is concluded in their research that this is due to an excitation of the second harmonic of the flumes resonant frequency.

4.4. Pressures and forces

Typical time histories for measured wave pressure and force are presented in Fig. 12 for all blocking fractions and selected wavelengths. The data do not exhibit a significant impulsive component; this is the anticipated response, as during the tests no waves were observed to break on or near the obstacle and there was little by way of slamming during the initial impact phase (Fig. 13). These results are significant because an impulsive component is instead specified in current recommended practice documents, such as FEMA (FEMA, 2012) and Okada et al. (2004). In the absence of wave force measurements under realistic tsunamis (here we exclude tests with simple solitary waves or those using dam-break bores), engineers writing design codes have taken the precautionary approach of biasing their advice towards loads from steep waves as generated in dam-break experiments, such as Nouri et al. (2010). and Al-Faesly et al. (2012), which often show impulsive loadings.

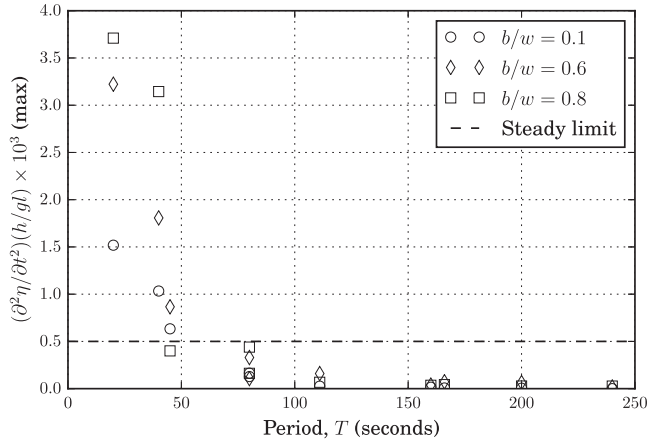

(a) Maximum values of $\frac{\partial^2\eta}{\partial t^2}\frac{h}{gl}$

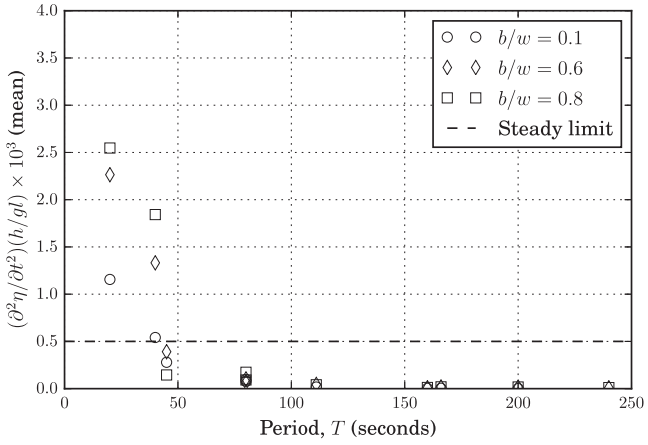

(b) Mean values of $\frac{\partial^2\eta}{\partial t^2}\frac{h}{gl}$

Fig. 10. Non-dimensional time derivatives $\frac{\partial^2 h}{\partial t^2}\frac{h}{gl}$ of wave elevation at the face of the building for all wave periods.

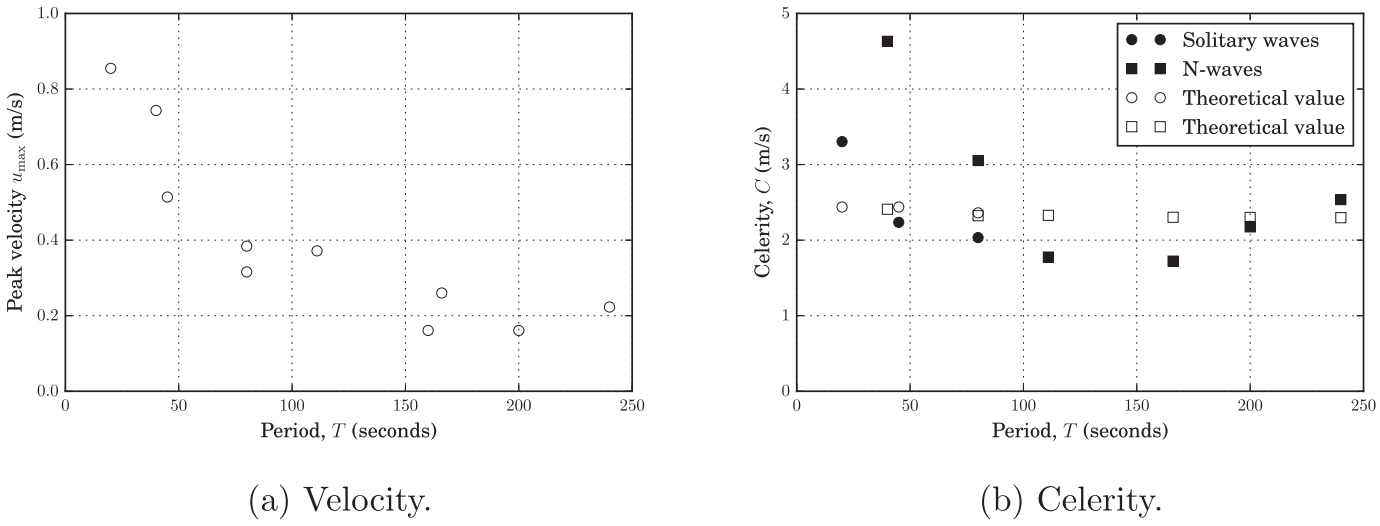

(a) Velocity. (b) Celerity.

Fig. 11. Variation of peak velocity u_{max} and wave celerity C with wave period.

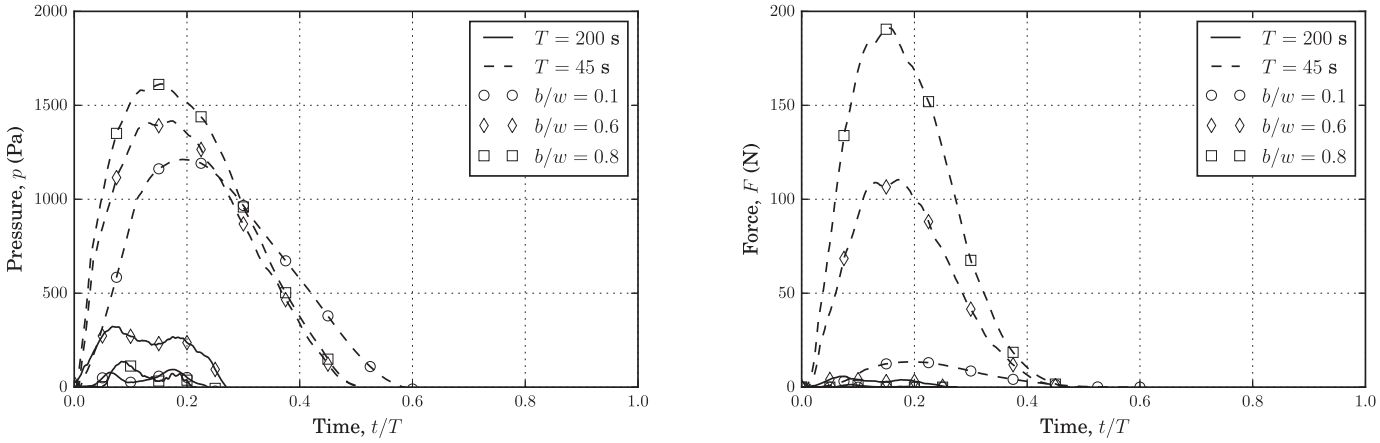

(a) Measured pressure (bottom gauge). (b) Measured force.

Fig. 12. Typical time histories of measured pressures and forces for a long ($T = 200$s) and short ($T = 45$s) N-waves.

Those experiments that use more realistic tsunami generation, for example those by Rossetto et al. (2011), Bremm et al. (2015), Allsop et al. (2014), Goseberg et al. (2013). and McGovern et al. (2017), have seldom if ever shown impulsive effects, suggesting that these more violent loadings may be significantly rarer than implied by dam-break studies.

The overall relationship between peak forces, pressures and wave period is presented in Fig. 14, which shows a pronounced attenuation of peak forces and pressures with increasing wave period. Fig. 15 traces peak pressures and forces with measured water height at the face of the obstacles. This figure shows that the measured forces are close to the corresponding hydrostatic force components. This is the anticipated response as predicted by the long wave theory presented in Section 2.

Applying the regime classification presented in Section 4.2, Fig. 16 shows that the majority of the measured pressures are hydrostatic, particularly in the unsteady regime. Results indicating pressures below the expected hydrostatic response are associated with the longest period waves with the lowest amplitudes; in these cases some of the water level fell below the measurement area of the pressure transducers, resulting in lower than expected pressure readings.

Fig. 17a shows the variation of drag coefficient with wave period, determined from the experiments as:

$$C_D = \lim_{Fr_1 \to 0} \frac{2\overline{F}_D}{\rho b u_1^2 h_1} \tag{22}$$

For longer period (>50 s), very shallow waves, there is significant scatter in the results which may be due to measured velocities being affected by high friction forces. This is reflected in Fig. 17b where a split in the data occurs, coinciding with the division of flow regimes. Results for wave periods exceeding 110 s have been omitted from this figure, as the very shallow water conditions resulted in unreliable velocity data readings. Since the focus of this research is on unsteady flow, only the data corresponding to wave periods less than 50 s be used to draw conclusions in subsequent sections of this paper. Using this subset of results, good agreement is achieved with the predictive equation for C_D (Eq. (19)), when a value of $C_{D0} = 1.9$ is used, which is the theoretical value for drag on a square cylinder in an unblocked turbulent flow.

5. Discussion and empirical closure

In this section, a modification of the empirical force equation originally proposed by Qi et al. (2014). for steady flow conditions is proposed for the application to unsteady flows, for which $\left(\frac{\partial^2 \eta}{\partial t^2}\right)\left(\frac{h}{gl}\right) > 0.5 \times 10^{-3}$,

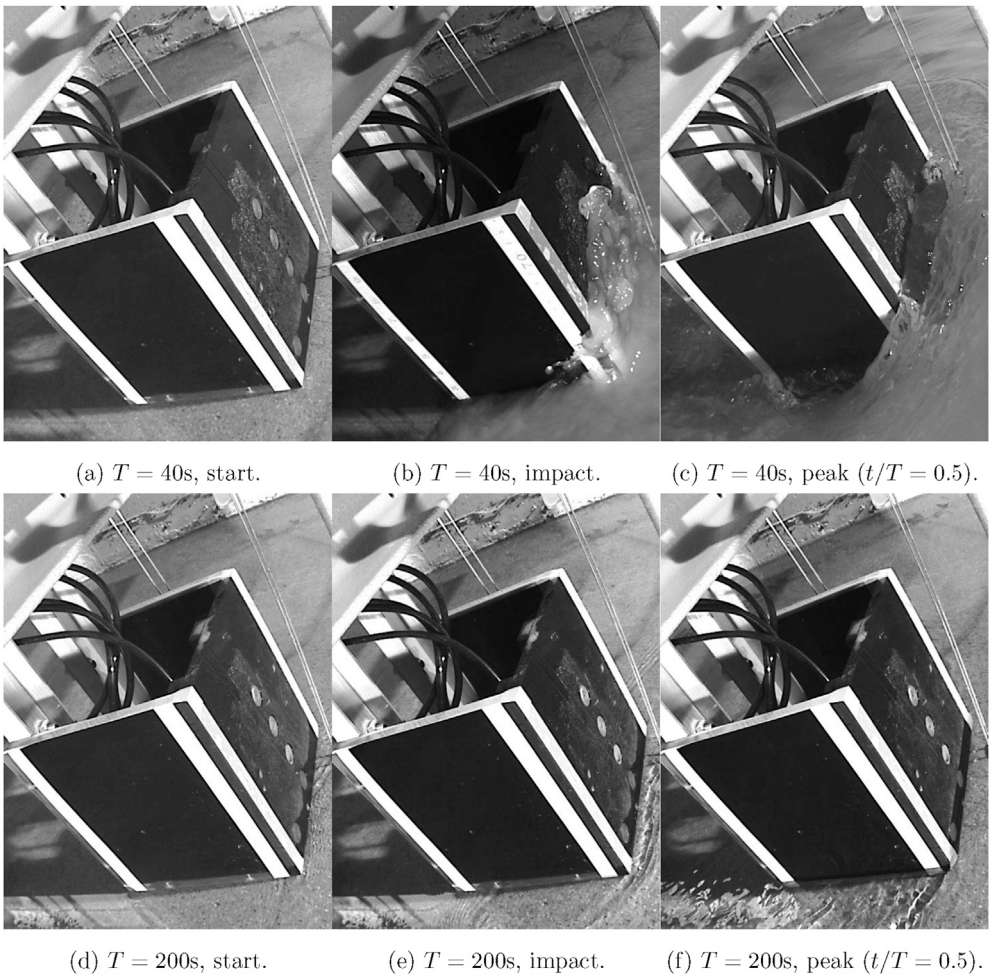

Fig. 13. Video stills of a short period ($T = 40$ s) and long period ($T = 200$ s) N-wave impacting an obstacle with a blocking fraction $b/w = 0.1$.

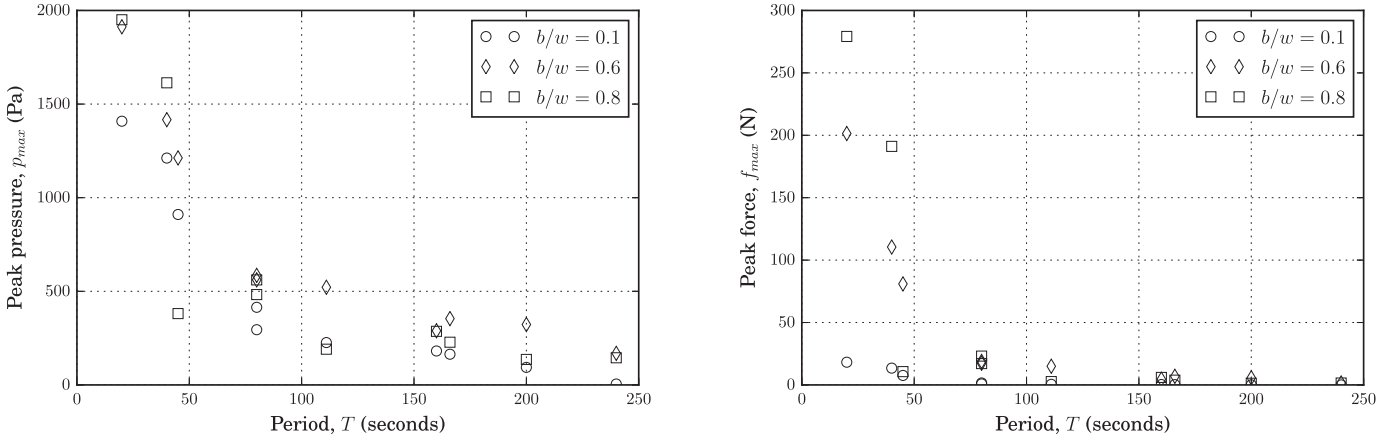

(a) Peak pressure. (b) Peak force.

Fig. 14. Variation of peak force and pressure with wave period for all obstacle widths.

based on the presented experiments. In Qi et al. (2014), and as implied by Eq. (10), a proportion of the total force experienced by the obstacle comes from drag and the remainder from hydrostatic effects. To reconcile these two force scalings, a general expression for $\overline{F}_D$ is proposed:

$$\overline{F}_D = \begin{cases} \frac{1}{2} C_D \rho b u_1^2 h_1 & \text{if} \quad Fr_2 < 1 \quad \text{(subcritical)} \\ \lambda \rho b g^{1/3} u_1^{4/3} h_1^{4/3} & \text{if} \quad Fr_2 \geq 1 \quad \text{(choked)} \end{cases} \tag{23}$$

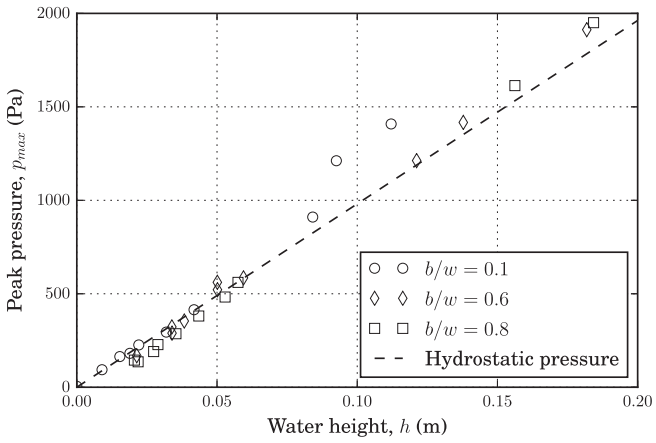

(a) Peak pressure.

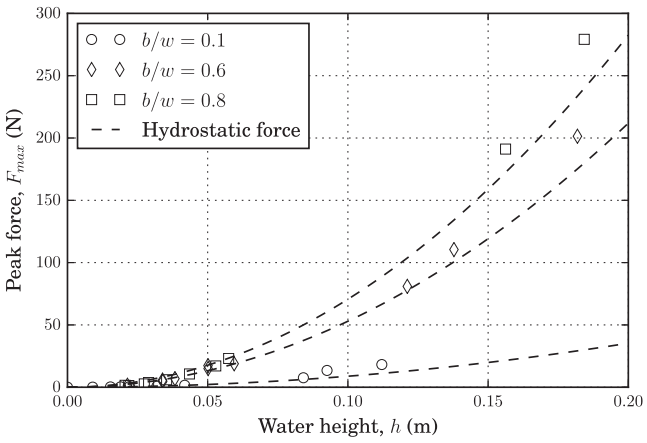

(b) Peak force.

Fig. 15. Variation of measured peak pressure and peak force with measured water height at the face of the obstacle.

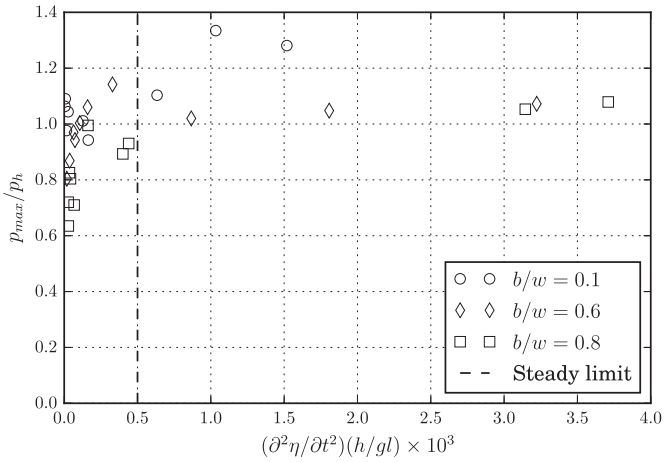

Fig. 16. Variation of non-dimensional peak pressure with non-dimensional time derivatives $\frac{\partial^2\eta}{\partial t^2}\frac{h}{gl}$ of wave elevation. $p_h = -\rho g h$ denotes the theoretical hydrostatic pressure.

in which:

$$\lambda = \frac{1}{2}C_D Fr_1^{2/3} + \frac{1}{2}C_H\left(\frac{1}{Fr_1^{4/3}} - \frac{1}{Fr_d^{4/3}}\right) \tag{24}$$

λ may be interpreted as an empirical closure for $\overline{F}_D$. For subcritical flow, the forces are due to drag alone as there is no appreciable difference in water height either side of the building, hence λ does not feature. Fr_d in λ is determined from the solution of Eq. (16). C_H is determined as per Qi et al. (2014) as $C_H = 2\overline{F}_D/\rho b g(h_1^2 - h_2^2)$. It should be noted that when Eq. (24) is being used in conjunction with time histories for u_1 and h_1, a discontinuity will arise in the force time history as the flow transitions from subcritical to choked regimes. To circumvent this, a cubic smoothing function can be applied in a similar manner to Petrone et al. (2016). Further, peak values of u_1 and h_1 are used in the determination of λ.

Fig. 18a and b shows the variation of λ with wave period and the non-dimensional measure of flow variability $\left(\frac{\partial^2\eta}{\partial t^2}\right)\left(\frac{h}{gl}\right)$, where $\left(\frac{\partial^2\eta}{\partial t^2}\right)\left(\frac{h}{gl}\right) > 0.5 \times 10^{-3}$; the relationship for both variables follows a similar pattern to that observed for C_D in Fig. 17.

Taking these computed values of λ and using them in $\overline{F}_D$ (Eq. (23)),

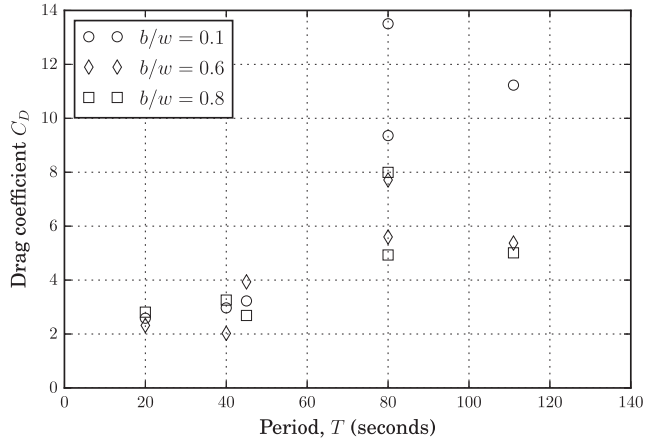

(a) Variation with period.

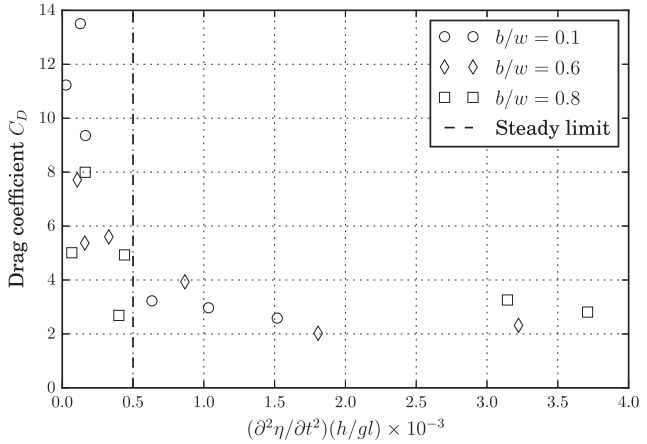

(b) Variation with $\frac{\partial^2\eta}{\partial t^2}\frac{h}{gl}$.

Fig. 17. Variation of measured drag coefficients C_D (a) period and (b) $\frac{\partial^2\eta}{\partial t^2}\frac{h}{gl}$.

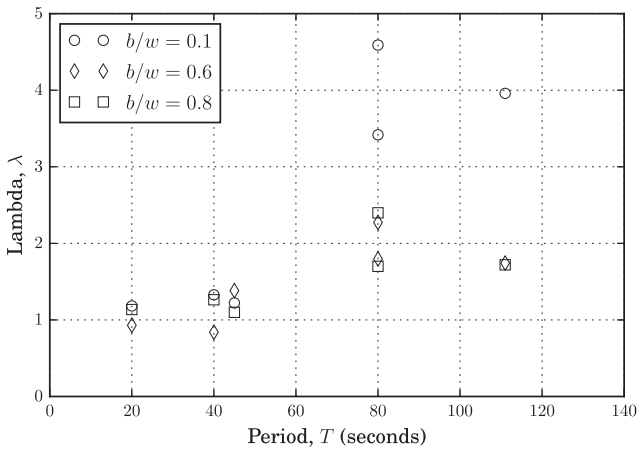

(a) Variation with period.

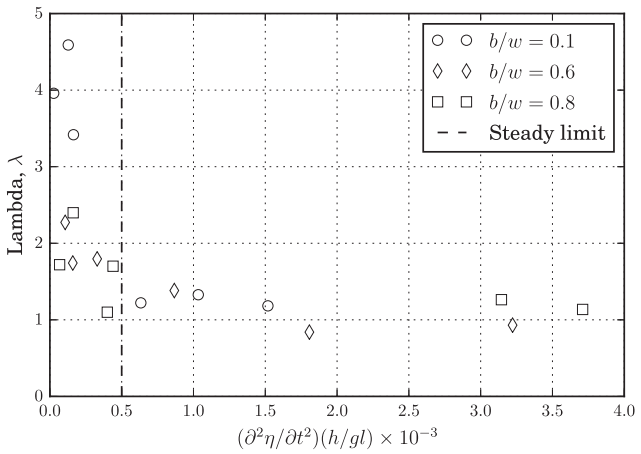

(b) Variation with $\frac{\partial^2\eta}{\partial t^2}\frac{h}{gl}$.

Fig. 18. Variation of derived force scaling coefficient λ with (a) period and (b) $\frac{\partial^2\eta}{\partial t^2}\frac{h}{gl}$.

their predictive capacity is assessed in Fig. 19. Agreement with laboratory results is acceptable, but there is potential for improvements with more reliable shallow water velocity measurements.

From both design and assessment perspectives, the blocking fraction (b/w) is an important parameter. For simplicity, it is desirable to make λ invariant to wave period or more generally $\left(\frac{\partial^2\eta}{\partial t^2}\right)\left(\frac{h}{gl}\right)$. With reference to Fig. 18b, λ tends to settle on a constant value, suggesting that an empirical closure taking only (b/w) into account is an acceptable balance between accuracy and utility. Considering only wave periods that are categorised in this research as unsteady, the relationship between λ and (b/w) is plotted in Fig. 20.

Using a least squares fit for λ as a polynomial function of (b/w), the following empirical closure for $\overline{F}_D$ is proposed:

$$\lambda = 1.37 - 1.35(b/w) + 1.37(b/w)^2 \tag{25}$$

which is applicable for unsteady flow regimes where $\left(\frac{\partial^2\eta}{\partial t^2}\right)\left(\frac{h}{gl}\right) > 0.5\times10^{-3}$. A summary of the force equations that are applicable to steady and unsteady inundation flows is presented in Table 3, with λ defined in Eq. (25) and λ_s corresponding to the steady flow defined by (Bahmanpour et al., 2017) as:

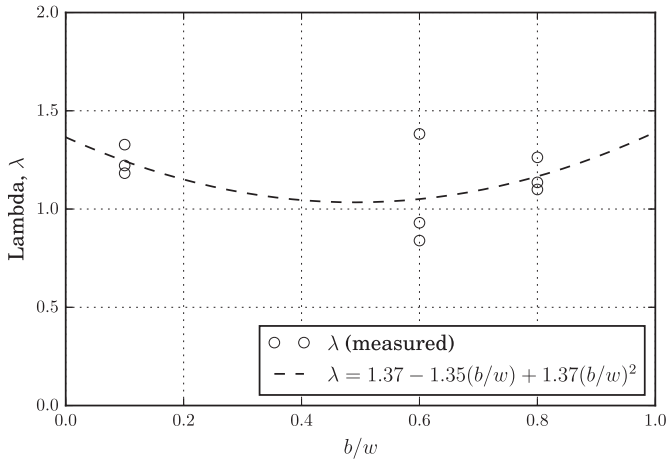

Fig. 20. Variation of derived and fitted force scaling coefficient λ with blocking fraction (b/w).

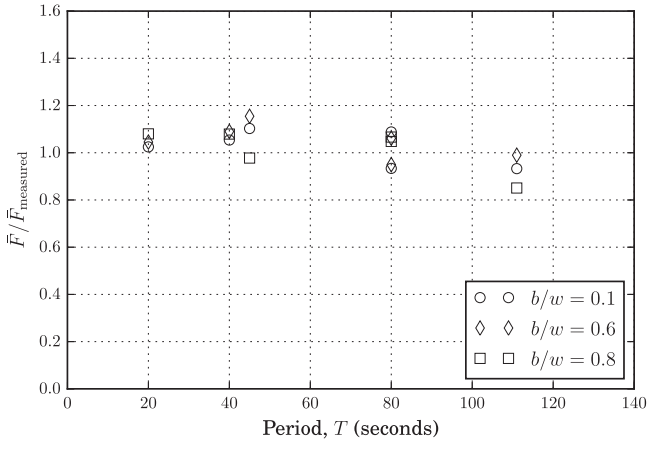

(a) Variation with period.

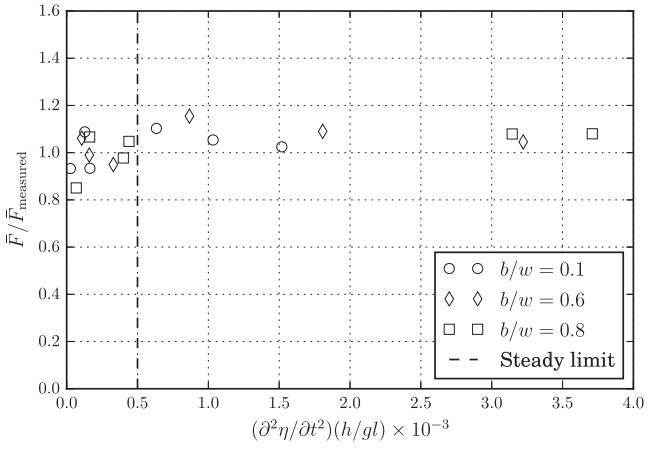

(b) Variation with $\frac{\partial^2\eta}{\partial t^2}\frac{h}{gl}$.

Fig. 19. Variation of predicted force $\overline{F}$ normalised by measured force F_{measured} with (a) period and (b) $\frac{\partial^2\eta}{\partial t^2}\frac{h}{gl}$.

Table 3
Summary equations for force $\overline{F}_D$ corresponding to steady and unsteady inundation flow regimes.

	Steady	Unsteady
	$\left(\frac{\partial^2\eta}{\partial t^2}\right)\left(\frac{h}{gl}\right) < 0.5\times10^{-3}$	$\left(\frac{\partial^2\eta}{\partial t^2}\right)\left(\frac{h}{gl}\right) \geq 0.5\times10^{-3}$
Subcritical, $Fr_2 < 1$	$\frac{1}{2}C_D\rho b u_1^2 h_1$	$\frac{1}{2}C_D\rho b u_1^2 h_1$
Choked, $Fr_2 \geq 1$	$\lambda_s b g^{1/3} u_1^{4/3} h_1^{4/3}$	$\lambda b g^{1/3} u_1^{4/3} h_1^{4/3}$

$$\lambda_s = 0.73 + 1.2(b/w) + 1.1(b/w)^2. \quad (26)$$

In determining the empirical closure specified by λ, the force acting on a building at any given location in the inundation flow can be determined by knowing only the Froude number and blocking fraction. The force equations proposed in this section can be adopted within current approaches to tsunami inundation modelling.

6. Concluding remarks

We describe an experimental study that seeks to examine the forces experienced by a rectangular obstacle in an unsteady free-surface channel flow. This study is one of a very limited number where prototype-like tsunami flows are simulated. In this study, the length of the obstacles are fixed and the blocking fraction (b/w) is allowed to vary from 0.1 to 0.8. A range of wave periods from 20 to 240 s are chosen and these encompass both solitary and trough-led wave forms.

The aims of this study are firstly to describe the evolution of pressures and forces of tsunami inundation flows around a single rigid rectangular object, and secondly, to develop a semi-empirical force equation in terms of offshore water height, flow velocity, blocking fraction, and Froude number with a view to being used in future design codes and numerical models.

The results show that for very long period waves encountering an idealised topography, the inundation flow can be considered to be gradually varying, to the extent that it can be considered steady. Through the introduction of obstacles in the form of buildings into the flow, it is evident that there is a strong interaction between obstacle widths and flow conditions, expressed in terms of the Froude number. When considering the temporal evolution of the forces and pressures, it is evident that for the wave periods under consideration, there is no impulsive component. Through classifying the impinging waves into steady and quasi-steady regimes, we demonstrate that the force parameterisation depends on both the upstream Froude number Fr_1 and the blocking fraction (b/w). Additionally, the effect of variations in the rate of change of flow $\left(\frac{\partial^2\eta}{\partial t^2}\right)\left(\frac{h}{gl}\right)$ appear to have a limited effect on the force parameterisation. Finally, the resulting pressure fields are observed to be hydrostatic, irrespective of flow regime. Therefore, in terms of preliminary recommendations for updated design guidance for the range of flow conditions investigated, the effect of impulsive forces may be neglected and the theoretical framework originally proposed by Qi et al. (2014). for quasi-steady flow conditions can be applied in a predictive capacity for certain unsteady inundation flows. Further experimental work that seeks to provide a detailed examination of the influence of topography and scale effects will be required to develop more generalised design guidance.

Acknowledgements

The research leading to these results has received funding from the European Research Council under the European Union's Seventh Framework Programme (FP7/2007–2013)/ERC grant agreement number 336084, awarded to Professor Tiziana Rossetto. The authors acknowledge the model-building support provided by Mr. David Kruup, University College London, as well as the provisions made by the technical staff at HR Wallingford. The authors are finally grateful to Dr. David McGovern, Dr. Ian Chandler, Dr. Crescenzo Petrone, Professor Ian Eames, Mr. Oliver Cook, Dr. Jonathan Gosaye Fida Kaba, Miss Roberta Riva, and Mr Alan Wright for their assistance in this research.

References

Al-Faesly, T., Palermo, D., Nistor, I., Cornett, A., 2012. Experimental modeling of extreme hydrodynamic forces on structural models. Int. J. Prot. Struct. 3 (4), 477–505.
Allsop, W., Chandler, I., Zaccaria, M., 2014. Improvements in the physical modelling of tsunamis and their effects. In: Proc. 5th Int. Conf. On Application of Physical Modelling to Port and Coastal Protection.
Arnason, A., Petroff, C., Yeh, H., 2009. Tsunami bore impingement onto a vertical column. J. Disaster Res. 4 (6), 391–403.
Asakura, R., Iwase, K., Ikeya, T., Takao, M., Keneto, T., Fujii, N., Ohmori, M., 2002. The tsunami wave force acting on land structures. In: Proceedings of the 28th International Conference on Coastal Engineering, Cardiff, Wales, pp. 1191–1202.
ASCE/SEI 7-16, 2017. Minimum Design Loads for Buildings and Other Structures.
Bahmanpour, A., Eames, I., Richardson, S., Rossetto, T., 2017. Computational study of the force and surface pressure on rectangular buildings in a steady free channel flow. J. Fluids Struct. (Submitted).
Borthwick, A.G.L., Ford, M., Weston, B.P., 2006. Solitary wave transformation, breaking and run-up at a beach. J. Marit. Eng. MA09, 1–9.
Bremm, G.C., Goseberg, N., Schlurmann, T., Nistor, I., 2015. Long wave flow interaction with a single square structure on a sloping beach. J. Mar. Sci. Eng. 3, 821–844.
Briggs, M.J., Synolakis, C.E., Harkins, G., Green, D.R., 1995. Laboratory experiments of tsunami runup on a circular island. Pure Appl. Geophys. 144, 569–593.
Chow, V.T., 1959. Open Channel Hydraulics. McGraw-Hill.
Cross, R.H., 1967. Tsunami surge forces. J. Waterw. Harbours Div. 93, 201–231.
Dargahi, B., 1989. Turbulent flow around a circular cylinder. Exp. Fluids 8 (1–2), 1–12.
Dean, R.G., Dalrymple, R.A., 1984. Water Wave Mechanics for Engineers and Scientists. World Scientific, London.
EEFIT, 2004. The Indian Ocean Tsunami of 26 December 2004: Mission Findings in Sri Lanka and Thailand. Institution of Structural Engineers. Tech. Rep.
EEFIT, 2009. The South Pacific Islands Earthquake and Tsunami of 29th September 2009: a Preliminary Field Report by EEFIT. Institution of Structural Engineers. Tech. Rep.
EEFIT, 2011. The Mw9.0 Tohoku Earthquake and Tsunami of 11th March 2011. Institution of Structural Engineers. Tech. Rep.
EEFIT, 2013. Recovery Two Years after the 2011 Tohoku Earthquake and Tsunami: a Return Mission Report by EEFIT. Institution of Structural Engineers. Tech. Rep.
Escande, L., 1939. Recherches sur l'ecoulement de l'eau entre les piles de ponts. Le. Genie Civ. 115, 1–10.
FEMA, 2012. FEMA P646: guidelines for design of structures for vertical evacuation from tsunamis. Appl. Technol. Counc.
Fenton, J.D., 2003. The effects of obstacles on surface levels and boundary resistance in open channels. In: Ganoulis, J., Prinos, P. (Eds.), Proc. 30th IAHR Congress.
Fenton, J.D., 2008. Obstacles in streams and their roles as hydraulic structures. In: Pagliara, S., Plus, E. (Eds.), Proc. 2nd International Junior Researcher and Engineer Workshop on Hydraulic Structures.
Fukui, Y., Nakamura, M., Shiraishi, H., 1963. Hydraulic study on tsunami. Coast. Eng. J. 6, 67–82.
Gauckler, P., 1867. Etudes Theoriques et Pratiques sur l'Ecoulement et le Mouvement des Eaux. Comptes Rendues l'Academie Sci. 64, 818–822.
Goseberg, N., Wurpts, A., Schlurmann, T., 2013. Laboratory-scale generation of tsunami and long waves. Coast. Eng. 79, 517–527.
Henderson, F.M., 1966. Open Channel Flow. Macmillan, New York.
Hornung, H.G., Willert, C., Turner, S., 1995. The flow field downstream of a hydraulic jump. J. Fluid Mech. 287, 299–316.
Hsieh, T., 1964. Resistance of cylindrical piers in open-channel flow. J. Hydraul. Div. 90, 161–173.
Imamura, F., Imteaz, M.A., 1995. Long waves in two layers: governing equations and numerical models. Sci. Tsunami Hazards 13 (1), 3–24.
Jensen, A., Pedersen, G.K., Wood, D.J., 2003. An experimental study of wave runup at a steep beach. J. Fluid Mech. 486, 161–188.
Lukkunaprasit, P., Thanaisathit, N., Yeh, H., 2009. Experimental verification of FEMA P646 tsunami loading. J. Disaster Res. 4 (6), 410–418.
Madsen, P.A., Fuhrman, D.R., Schaffer, H.A., 2008. On the solitary wave paradigm for tsunamis. J. Geophys. Res. 113 (C12) n/a–n/a.
Manning, R., 1891. On the flow of water in open channels and pipes. Trans. Inst. Civ. Eng. Irel. 20, 161–207.
McGovern, D.J., Rossetto, T., Allsop, W., 2016. Experimental Impact of Scaled Tsunami Waves on Vertical Sea Walls in preparation.
McGovern, D.J., Chandler, I., Allsop, W., Robinson, T., Rossetto, T., 2017. Pneumatic long-wave simulation of tsunami-length waveforms and their runup (under review). Coast. Eng. 1–23.
Miles, J.W., 1980. Solitary waves. Annu. Rev. Fluid Mech. 12, 11–43.
Montes, S., 1998. Hydraulics of Open Channel Flow. ASCE, New York.
Nakamura, S., Tsuchiya, Y., 1973. On shock pressure of surge on a wall. Bull. Disaster Prev. Res. Inst. Kyoto Univ. 3–4 (12), 47–58.
Nouri, Y., Nistor, I., Palermo, D., 2010. Experimental investigation of tsunami impact on free standing structures. Coast. Eng. J. 52 (1), 43–70.

Okada, T., Sugano, T., Ishikawa, T., Ogi, T., Takai, S., Hamabe, T., 2004. Structural Design Method of Building to Seismic Sea Wave. The Building Center of Japan (in Japanese), Tech. Rep.
Petrone, C., Rossetto, T., Goda, K., 2016. Fragility Assessment of a RC Structure Under Tsunami Actions via Nonlinear Static and Dynamic Analyses under review for Engineering Structures.
Qi, Z.X., Eames, I., Johnson, E.A., 2014. Force acting on a square cylinder fixed in a free-surface channel flow. J. Fluid Mech. 756, 716–727.
Ramsden, J.D., 1993. Tsunamis: Forces on a Vertical Wall Caused by Long Waves, Bores, and Surges on a Dry Bed. California Institute of Technology. Ph.D. thesis.
Ramsden, J.D., Raichlen, F., 1990. Forces on vertical wall caused by incident bores. J. Waterw. Port Coast. Ocean Eng. 116 (5), 592–613.
Ranga Raju, K.G., Rana, O.P.S., Asawa, G.L., Pillai, A.S.N., 1983. Rational assessment of blockage effect in channel flow past smooth circular cylinders. J. Hydral. Res. 21, 289–302.
Reinauer, R., Hager, W.H., 1994. Supercritical flow behind chute piers. J. Hydral. Eng. 120 (11), 1292–1308.
Reynolds, O., 1903. Papers on Mechanical and Physical Subjects, vol. 3. The Sub-Mechanics of the Universe, Cambridge University Press.
Ritter, A., 1892. Die Fortpflanzung der Wasserwellen. Z. Des. Vereines Dtsch. Ingenieure 36, 947–954.
Rossetto, T., Allsop, W., Charvet, I., Robinson, D.I., 2011. Physical modelling of tsunami using a new pneumatic wave generator. Coast. Eng. 58, 517–527.
Sadeque, M.A.F., Rajaratnam, N., Loewen, M.R., 2008. Flow around cylinders in open channels. J. Eng. Mech. 134 (1), 60–71.
Svendsen, I.A., Veeramony, J., Bakunin, J., 2000. The flow in weak turbulent hydraulic jumps. J. Fluid Mech. 418, 25–57.
Synolakis, C.E., 1987. The run-up of solitary waves. J. Fluid Mech. 185, 523–545.
Synolakis, C.E., Bernard, E.N., Titov, V.V., Kanoglu, U., Gonzalez, F.I., 2008. Validation and verification of tsunami numerical models. Pure Appl. Geophys. 165, 2197–2228.
Tadepalli, S., Synolakis, C.E., 1994. The run-up of N-waves on sloping beaches. In: Proceedings of the Royal Society of London: Mathematical and Physical Sciences, A445, pp. 99–112.
Tadepalli, S., Synolakis, C.E., 1996. Model for the leading waves of tsunamis. Phys. Rev. Lett. 77, 2141–2144.
Tamura, T., Miyagi, T., 1999. The effect of turbulence on aerodynamic forces on a square cylinder with various corner shapes. J. Wind Eng. Ind. Aerod. 83 (1–3), 135–145.
Thusyanthan, N., Madabhushi, M., 2008. Tsunami wave loading on coastal houses: a model approach. Proc. Inst. Civ. Eng. - Civ. Eng. 161, 77–86.
Vallis, G.K., 2006. Atmospheric and Oceanic Fluid Dynamics: Fundamentals and Large-scale Circulation. Cambridge University Press.
Yeh, H., Ghazali, H., Marton, I., 1989. Experimental study of bore run-up. J. Fluid Mech. 206, 563–578.